

Solving Bilinear Inverse Problems using Deep Generative Priors

Muhammad Asim*

Fahad Shamshad*

Ali Ahmed

*The authors have contributed equally to this work.

Department of Electrical Engineering, Information Technology University,
Lahore, Pakistan.

{msee16001, fahad.shamshad, ali.ahmed}@itlu.edu.pk

Abstract

This paper proposes a new framework to handle the bilinear inverse problems (BIPs): recover \mathbf{w} , and \mathbf{x} from the measurements of the form $\mathbf{y} = \mathcal{A}(\mathbf{w}, \mathbf{x})$, where \mathcal{A} is a bilinear operator. The recovery problem of the unknowns \mathbf{w} , and \mathbf{x} can be formulated as a non-convex program. A general strategy is proposed to turn the ill-posed BIP to a relatively well-conditioned BIP by imposing a structural assumption that \mathbf{w} , and \mathbf{x} are members of some classes \mathcal{W} , and \mathcal{X} , respectively, that are parameterized by unknown latent low-dimensional features. We learn functions mapping from the hidden feature space to the ambient space for each class using generative models. The resulting reduced search space of the solution enables a simple alternating gradient descent scheme to yield promising result in solving the non-convex BIP.

To demonstrate the performance of our algorithm, we choose an important BIP; namely, blind image deblurring as a motivating application. We show through extensive experiments that this technique shows promising results in deblurring images of real datasets and is also robust to noise perturbations.

1. Introduction

This paper considers recovering unknown vectors \mathbf{w} , and \mathbf{x} from observation $\mathbf{y} = \mathcal{A}(\mathbf{w}, \mathbf{x})$ collected through a bilinear operator \mathcal{A} . In its full generality, the inverse problem is severely ill-posed as many different instances of \mathbf{x} , and \mathbf{w} fit the observations. We study image deblurring; an important bilinear inverse problem (BIP) in computer vision, and image processing, where one wants to recover an image \mathbf{x} by observing $\mathbf{y} = \mathbf{w} * \mathbf{x}$; its convolution with a blur kernel \mathbf{w} . In other words, the bilinear map is simply

$$\mathcal{A}(\mathbf{w}, \mathbf{x}) := \mathbf{w} * \mathbf{x}. \quad (1)$$

In its full generality, recovering the true \mathbf{x} is impossible as the mapping from inputs \mathbf{w} , and \mathbf{x} to \mathbf{y} is many-to-one, and

not only that, the natural formulation of BIP as an optimization program

$$\underset{\mathbf{w}, \mathbf{x}}{\text{minimize}} \|\mathbf{y} - \mathbf{w} * \mathbf{x}\|_2^2 \quad (2)$$

is non-convex. We assume that \mathbf{w} , and \mathbf{x} are not completely arbitrary but are members of some structured classes such as motion or Gaussian blurs, and natural images, respectively. Such natural classes can often be mapped to small vectors lying in a low-dimensional feature space using some unknown (possibly non-linear) generator maps. Our general strategy is to learn this generator map for each of the class using powerful deep generative networks. These generator maps introduce additional very pertinent constraints in (2) leading to a more well-conditioned BIP. We then use an alternating gradient descent scheme on the latent low-dimensional feature vectors of each of the unknowns to minimize the objective (2). We show that this strategy reliably recovers \mathbf{w} , and \mathbf{x} . For illustration, we present the result of our algorithm using extensive experiments on real image datasets.

The ill-posed nature of BIPs manifests itself even in the simplest bilinear map \mathcal{A} that returns pointwise products of the respective entries of vectors \mathbf{w} , and \mathbf{x} , that is, $\mathcal{A}(\mathbf{w}, \mathbf{x}) = \mathbf{w} \odot \mathbf{x}$. It is clear that any pair $(\alpha\mathbf{w}, \alpha^{-1}\mathbf{x})$ for some scalar multiple $\alpha \neq 0$ constitutes a solution. We consider a classical bilinear inverse problem in signal processing, and computer vision, where observations are the convolution of unknowns \mathbf{w} , and \mathbf{x} as in (1). Evidently, the map \mathcal{A} is many-to-one due to ambiguities caused by scalings, and translations of the inputs. We take $\mathbf{x} \in \mathbb{R}^L$, and $\mathbf{w} \in \mathbb{R}^L$ to be members of some structured classes \mathcal{W} , and \mathcal{X} , respectively, such that every $\mathbf{x} \in \mathcal{X}$, and $\mathbf{w} \in \mathcal{W}$ can be characterized by a latent low-dimensional feature vector. Mathematically, we can write a $\mathbf{w} \in \mathcal{W}$, and $\mathbf{x} \in \mathcal{X}$ as

$$\mathbf{w} = \mathcal{B}(\mathbf{h}), \quad \text{and} \quad \mathbf{x} = \mathcal{C}(\mathbf{m}) \quad (3)$$

for some unknown vectors $\mathbf{h} \in \mathbb{R}^K$, and $\mathbf{m} \in \mathbb{R}^N$, and unknown feature maps (possibly non-linear) $\mathcal{B} : \mathbb{R}^K \rightarrow$

\mathbb{R}^L , and $\mathcal{C} : \mathbb{R}^N \rightarrow \mathbb{R}^L$, where $K, N < L$. The unknown generator maps \mathcal{B} , and \mathcal{C} are discovered using generative models trained to learn the distribution $p_{\mathcal{W}}$, and $p_{\mathcal{X}}$ of the class \mathcal{W} , and \mathcal{X} , respectively. This is accomplished, for example, by training the weights of a generative adversarial networks (GAN) for each of the classes using representative training data $\{\mathbf{w}_q \in \mathcal{W}\}_{q=1}^Q$ and $\{\mathbf{x}_r \in \mathcal{X}\}_{r=1}^R$ of the classes \mathcal{W} , and \mathcal{X} , respectively. After training, we fix the weights of GAN for each class and get generative maps \mathcal{B} , and \mathcal{C} by forward pass through these GANs models.

The trained generator maps \mathcal{B} , and \mathcal{C} provide a mapping from the latent low-dimensional vectors \mathbf{h} , and \mathbf{m} to the ambient high dimensional objects $\mathbf{w} \in \mathcal{W}$, and $\mathbf{x} \in \mathcal{X}$, respectively. With \mathcal{B} , and \mathcal{C} fixed, the BIP now reduces to finding the corresponding \mathbf{h} , and \mathbf{m} that fit the observational model

$$\mathbf{y} = \mathcal{B}(\mathbf{h}) * \mathcal{C}(\mathbf{m}) \quad (4)$$

derived from (1). In other words, we now fix the weights of the GANs and tweak the low-dimensional inputs to fit the model in (4). Trained generators \mathcal{B} , and \mathcal{C} reduce the number of unknown from $2L$ to only $K + N$, and a natural formulation of the inverse problem as an optimization program is as follows

$$\underset{\mathbf{h}, \mathbf{m}}{\text{minimize}} \|\mathbf{y} - \mathcal{B}(\mathbf{h}) * \mathcal{C}(\mathbf{m})\|_2^2 + \lambda f(\mathbf{h}) + \gamma g(\mathbf{m}) \quad (5)$$

where the first term is the observation fitting term; and $f : \mathbb{R}^L \rightarrow \mathbb{R}$, and $g : \mathbb{R}^L \rightarrow \mathbb{R}$ are convex penalty functions, and $\lambda, \gamma \geq 0$ are adjustable weighting parameters. We choose f and g to be the standard ℓ_2 norms. Owing to the multiplicative constraint in the fitting term, the optimization program in (5) is non-convex. A gradient descent scheme is employed to minimize the non-convex objective in \mathbf{h} , and \mathbf{m} alternately to arrive at a local minima $(\hat{\mathbf{h}}, \hat{\mathbf{m}})$. Given the low-dimensional representations $\hat{\mathbf{h}}$, and $\hat{\mathbf{m}}$, we use a forward pass through the trained generator to recover the estimated blur kernel $\hat{\mathbf{w}} = \mathcal{B}(\hat{\mathbf{h}})$, and the image $\hat{\mathbf{x}} = \mathcal{C}(\hat{\mathbf{m}})$ in (1).

Our proposed approach applied to the important blind image deblurring problem in computer vision, and image processing produces the results shown in Figure 1. It showcases deblurring achieved by our algorithm on two datasets. For illustration, we also compare our results with a contemporary dark prior [26] technique; our results are perceptually much better than [26] and as will be shown in experimental section, highly robust to noise and large blurs when compared to convolutional neural network (CNN)[12]. The image \mathbf{x} comes from a general class \mathcal{X} of, for example, celebrity faces (CelebA)[22] or street house number images (SVHN) [24]. Similarly, the blur \mathbf{w} comes from a general class \mathcal{W} of various motion and Gaussian blurs. We train generative models including adversarial networks and variational autoencoders using training data from each class. The

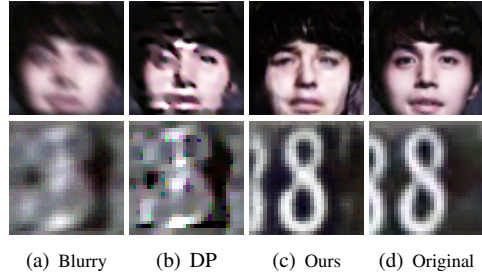


Figure 1: Images from SVHN and CelebA data set (a) shows blurry image. (b) shows image recovered by dark prior (DP) [26] approach. (c) shows our recovered images and original images are shown in (d).

trained models are then fixed and act as a mapping \mathcal{B} , and \mathcal{C} from the low-dimensional feature to ambient dimension. We then solve the non-convex optimization program in (5) to find out the feature vectors \mathbf{h} , and \mathbf{m} that best explain the blurred image \mathbf{y} . The resulting feature vectors are then used to generate a deblurred image $\mathbf{x} = \mathcal{C}(\mathbf{m})$ in the range of the generator \mathcal{C} .

1.1. Main Contribution

Main contribution of our work is the combination of the powerful idea of generative models with bilinear inverse problems for the first time. We show through extensive experiments that using generative models for a reformulation of the ill-posed bilinear inverse problem from ambient to a latent lower dimension paves the way for a more well conditioned inverse problem. The resultant problem can be effectively solved using an alternating gradient descent scheme yielding promising results in image deblurring on real datasets. It also turns out that using generative maps induces a very strong prior, highly robust to noise and extravagant blurs.

The rest of the paper is organized as follows. In Section 1.2 gives an overview of the related work. In Section 2, we give a brief recap of the functionality of generative models followed by Section 3 that describes alternating gradient descent scheme for image deblurring in the feature space. Section 4 contains experimental results. In Section 5, we discuss limitation and challenges of proposed algorithm followed by concluding remarks.

1.2. Related Work

BIPs have been studied extensively in signal processing and machine learning literature in the context of various motivating applications such as blind channel estimation in wireless communication [20], dictionary learning [31], phase retrieval [6, 15], and matrix factorization [8]. One interesting direction of future work is to extend the general strategy laid out in this paper to BIPs (mentioned above)

other than the image deblurring problem in focus here.

Recently, some exciting new convex relaxations to solve BIP have been proposed [3, 2, 1]. Additional linear constraints are introduced in these approaches by assuming that the unknowns \mathbf{w} , and \mathbf{x} live in known subspaces to find the true solution. In this aspect, our strategy is similar as we also make the problem well conditioned by imposing that the unknowns lie in the range of the non-linear generator maps \mathcal{B} , and \mathcal{C} , not known in advance. A gradient descent scheme to handle the non-convex objective in the blind deconvolution problem was analyzed in [21]. We implement a similar gradient descent scheme over the trained generative models.

Blind image deblurring has been studied thoroughly and in general, various additional penalties exploiting structure of the image or blur kernel are introduced to circumvent the ill-posedness. These natural structures include images or blur kernel expected to be sparse in some transform domain; see, for example, [7, 9, 19, 13, 35, 5]. Another approach [13, 35] more directly comparable to ours is to learn an over complete dictionary for sparse representation of image patches. Instead of linear representation of the image in dictionary, we are learning a more powerful non-linear mapping of full size images to a low-dimensional feature space, and we directly solve a gradient decent scheme to deblur the image instead of first finding a sparse representation. This leads to a clean, and simple strategy leading to much better deblurring results. Some of the other penalty functions to improve the conditioning of the problem are low-rank, and total variation based priors on image patches, and image gradients [25, 28]. Another recently introduced prior that seems to outperform other techniques for deblurring is the dark channel prior [26] which makes a prior assumption on the sparsity of dark channel of blurred image and incorporate this information in optimization problem of half-quadratic splitting L_0 minimization approach [33]. Therefore, we choose to compare our results with dark prior (DP) as in Figure 1.

Deep learning has emerged as the new state of the art in blind image deconvolution. The results so far focus on bypassing the blur kernel estimation, and training a network to deblur on a series of blurry and corresponding clean images; see, for example, [12, 23]. The main drawback of this approach is that even for a single image, the neural network has to learn to deblur it against all blurs under consideration, and when there are more than one image, the training examples should somehow scale with the product of the dimension of the features of image and blur. This leads to far too many training examples to have for any hope of producing competitive deblurring results with such techniques. On the other hand, we train separate generative models for images and blurs, and solve an iterative deblurring algorithm to deblur. This approach makes our deblurring robust to

large blurs and noise, as will be shown in the experimental results. Moreover, our approach is readily adaptable for different blur models, as the blur training is independent of images unlike recently proposed blind image deblurring approaches [30, 34].

2. Generative Models

The generative maps \mathcal{B} , and \mathcal{C} for the class \mathcal{W} , and \mathcal{X} will be acquired using powerful techniques of generative models; namely, the generative adversarial network (GAN) [11] and variational autoencoder (VAE) [17].

Generative Adversarial Network: As the generative adversarial networks (GANs) are known to produce relatively more crisp, and realistic looking images; therefore, for the face dataset a GAN is trained to learn the generator map $\mathcal{C} : \mathbb{R}^N \rightarrow \mathbb{R}^L$. The training process involves two neural networks, namely, a generator \mathcal{G} (proxy for \mathcal{C}), and a discriminator $\mathcal{D} : \mathbb{R}^L \rightarrow \mathbb{R}$ that given a sample \mathbf{x} returns the probability of it coming from \mathcal{X} . The role of \mathcal{D} is to assist \mathcal{G} in learning the distribution $p_{\mathcal{X}}$ of data \mathcal{X} by evaluating the samples generated by \mathcal{G} . The minimax objective is formulated as [11]

$$\min_{\mathcal{G}} \max_{\mathcal{D}} \mathbb{E}_{\mathbf{x} \sim p_{\mathcal{X}}} \log \mathcal{D}(\mathbf{x}) + \mathbb{E}_{\mathbf{m} \sim p_{\mathcal{N}}} \log(1 - \mathcal{D}(\mathcal{G}(\mathbf{m}))),$$

where optimizing over \mathcal{G} , and \mathcal{D} alludes to tweaking the parameters (weights) of both neural nets until an equilibrium between \mathcal{D} , and \mathcal{G} is attained. The low-dimensional feature vector $\mathbf{m} \in \mathbb{R}^K$ comes from a normal distribution $p_{\mathcal{N}}$. For more details; see, [10]. The optimal \mathcal{G} is our generator map \mathcal{C} .

Variational Autoencoder: We use variational autoencoder (VAE) to learn the generator maps \mathcal{B} for the blur kernels, and \mathcal{C} for the MNIST and SVHN image data sets. The loss function to train, for example, the generator map \mathcal{B} of the blur dataset \mathcal{W} is explicitly stated as follows [17]

$$\mathbb{E} [\log(p_{\mathcal{W}|\mathcal{N}}(\mathbf{w}|\mathbf{h})) + \text{KL}[p_{\mathcal{N}|\mathcal{W}}(\mathbf{h}|\mathbf{w})||p_{\mathcal{N}}(\mathbf{h})]]$$

where KL is the Kullback-Leibler distance measure. First term in the above expression maximizes the probability of generating a blur \mathbf{w} that is representative of the class \mathcal{W} given a low-dimensional feature vector \mathbf{h} coming from a normal distribution, and the second term ensures that the distribution from ambient to the latent dimension behaves like a normal distribution. In this process a decoder is trained that acts as a generator \mathcal{B} that maps a small feature vector \mathbf{h} to large \mathbf{w} in the class \mathcal{W} .

In an exactly similar manner, using a VAE, one can train a generator map \mathcal{C} for the class \mathcal{X} .

2.1. Recovery via Backpropagation:

Given the generator map \mathcal{C} , a simple and naive strategy for deblurring could be to take the blurred image and recover a closest image in the range of \mathcal{C} . Mathematically,

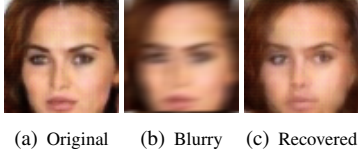


Figure 2: (a) shows original image with its blurred version shown in (b). This blurred image is back propagated to find the closest image shown in (c) in the range of generator.

this would amount to minimizing the objective function $\|\mathbf{y} - \mathcal{C}(\mathbf{m})\|_2^2$ w.r.t. \mathbf{m} . As the weights of the generator \mathcal{C} are already fixed after training, a local minimizer $\hat{\mathbf{m}}$ can be attained using back propagation over the generator neural network \mathcal{C} . The recovered image $\hat{\mathbf{x}}$ is then just a forward pass through \mathcal{C} , i.e., $\hat{\mathbf{x}} = \mathcal{C}(\hat{\mathbf{m}})$. Figure 2 demonstrates that this approach does not succeed in recovering a good enough replica of the original images in blind image deblurring problem.

3. Alternating Gradient Descent

Since we are interested in the optimization program in (5), we now present an alternating gradient descent approach to achieve a local minima of the loss function:

$$\mathcal{L}(\mathbf{h}, \mathbf{m}) := \|\mathbf{y} - \mathcal{B}(\mathbf{h}) * \mathcal{C}(\mathbf{m})\|_2^2 + \lambda \|\mathbf{h}\|_2^2 + \gamma \|\mathbf{m}\|_2^2 \quad (6)$$

The gradient expressions will be easier to handle in the Fourier domain. Let \mathbf{F} be the DFT matrix with entries

$$\mathbf{F}[\omega, n] = \frac{1}{\sqrt{L}} e^{-i 2 \pi \omega n}, \quad (\omega, n) \in [L] \times [L].$$

Assuming that $*$ denotes the circular convolution, the loss \mathcal{L} can be transformed in the frequency domain to yield

$$\|\mathbf{y} - \mathcal{B}(\mathbf{h}) * \mathcal{C}(\mathbf{m})\|_2^2 = \|\mathbf{Fy} - \sqrt{L} \mathbf{F} \mathcal{B}(\mathbf{h}) \odot \mathbf{F} \mathcal{C}(\mathbf{m})\|_2^2, \quad (7)$$

where \odot represents the standard Hadamard product. Let $\nabla_{\mathbf{h}} \mathcal{L}$, and $\nabla_{\mathbf{m}} \mathcal{L}$ denote the Wirtinger gradients of $\mathcal{L}(\mathbf{h}, \mathbf{m})$ w.r.t. the feature vectors \mathbf{h} , and \mathbf{m} , respectively, and $\eta \in \mathbb{R}$ be the step size. The alternating gradient descent algorithm to minimize the loss term in (6) is given in Algorithm 1 below. The number of iterations can either be specified in advance or one can continue until the gradient norm are small enough.

We now explicitly compute the Wirtinger gradient¹ expressions $\nabla_{\mathbf{h}} \mathcal{L}$, and $\nabla_{\mathbf{m}} \mathcal{L}$. Define residual \mathbf{r}_t at the t th

¹ For a function $f(\mathbf{z})$ of variable $\mathbf{z} = \mathbf{u} + i\mathbf{v}$, the Wirtinger derivatives of $f(\mathbf{z})$ with respect to \mathbf{z} , and $\bar{\mathbf{z}}$ are defined as

$$\frac{\partial f}{\partial \mathbf{z}} = \frac{1}{2} \left(\frac{\partial f}{\partial \mathbf{u}} - i \frac{\partial f}{\partial \mathbf{v}} \right), \quad \text{and} \quad \frac{\partial f}{\partial \bar{\mathbf{z}}} = \frac{1}{2} \left(\frac{\partial f}{\partial \mathbf{u}} + i \frac{\partial f}{\partial \mathbf{v}} \right)$$

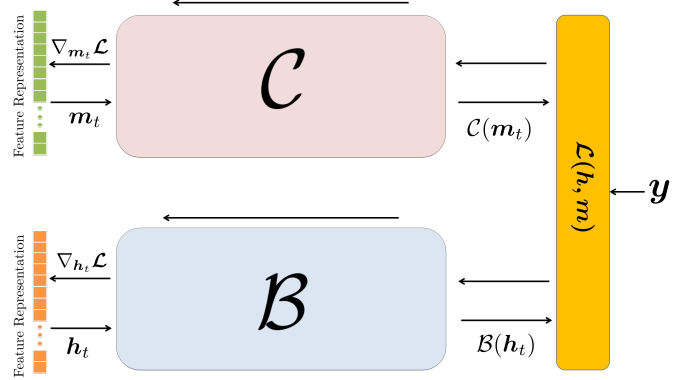


Figure 3: For each estimate of \mathbf{m}_t and \mathbf{h}_t , the gradients $\nabla_{\mathbf{h}} \mathcal{L}$ and $\nabla_{\mathbf{m}} \mathcal{L}$ for next update are evaluated by simply backpropagating the loss $\mathcal{L}(\mathbf{h}, \mathbf{m})$ in (6) through both the blur generator \mathcal{B} and image generator \mathcal{C} respectively.

Algorithm 1 Alternating Gradient Descent

Input: \mathbf{y} , \mathcal{B} , \mathcal{C} and η
Output: Estimates $\hat{\mathbf{x}}$ and $\hat{\mathbf{h}}$
Initialize:
 $\mathbf{m}_0 := \underset{\mathbf{m}}{\operatorname{argmin}} \|\mathbf{y} - \mathcal{C}(\mathbf{m})\|_2^2, \quad \mathbf{h}_0 := \mathcal{N}(\mathbf{0}, \mathbf{I}_K)$
for $t = 1, 2, 3, \dots$ **do**
 $\quad \mathbf{h}_t \leftarrow \mathbf{h}_{t-1} - \eta \nabla_{\mathbf{h}_{t-1}} \mathcal{L}(\mathbf{h}_{t-1}, \mathbf{m}_{t-1});$
 $\quad \mathbf{m}_t \leftarrow \mathbf{m}_{t-1} - \eta \nabla_{\mathbf{m}_{t-1}} \mathcal{L}(\mathbf{h}_{t-1}, \mathbf{m}_{t-1});$
end for
 $\hat{\mathbf{w}} \leftarrow \mathcal{B}(\mathbf{h}_t), \quad \hat{\mathbf{x}} \leftarrow \mathcal{C}(\mathbf{m}_t)$

iteration:

$$\mathbf{r}_t := \mathbf{F} \mathcal{B}(\mathbf{h}_t) \odot \sqrt{L} \mathbf{F} \mathcal{C}(\mathbf{m}_t) - \mathbf{Fy},$$

where $\dot{\mathcal{B}}_{\mathbf{h}} = \frac{\partial}{\partial \mathbf{h}} \mathcal{B}(\mathbf{h})$, $\dot{\mathcal{C}}_{\mathbf{m}} = \frac{\partial}{\partial \mathbf{m}} \mathcal{C}(\mathbf{m})$. Then, it is easy to see that

$$\begin{aligned} \nabla_{\mathbf{h}_t} \mathcal{L}(\mathbf{h}_t, \mathbf{m}_t) &= \dot{\mathcal{B}}_{\mathbf{h}_t}^* \mathbf{F}^* [\mathbf{r}_t \odot \sqrt{L} \mathbf{F} \mathcal{C}(\mathbf{m}_t)] + \lambda \mathbf{h}_t, \\ \nabla_{\mathbf{m}_t} \mathcal{L}(\mathbf{h}_t, \mathbf{m}_t) &= \sqrt{L} \dot{\mathcal{C}}_{\mathbf{m}_t}^* \mathbf{F}^* [\mathbf{r}_t \odot \mathbf{F} \mathcal{B}(\mathbf{h}_t)] + \gamma \mathbf{m}_t. \end{aligned}$$

For illustration, take the example of a two layer generator map \mathcal{B} , which is simply

$$\mathcal{B}(\mathbf{h}) = \text{relu}(\mathbf{B}_2(\text{relu}(\mathbf{B}_1 \mathbf{h}))),$$

where $\mathbf{B}_1 : \mathbb{R}^{L_1 \times K}$, and $\mathbf{B}_2 : \mathbb{R}^{L \times L_1}$ are the weight matrices at the first, and second layer, respectively. In this case $\dot{\mathcal{B}}_{\mathbf{h}} = \widetilde{\mathcal{B}}_{2,h} \widetilde{\mathcal{B}}_{1,h}$ where $\widetilde{\mathcal{B}}_{1,h} = \text{diag}(\mathbf{B}_1 \mathbf{h} > 0) \mathbf{B}_1$ and $\widetilde{\mathcal{B}}_{2,h} = \text{diag}(\mathbf{B}_2 \widetilde{\mathcal{B}}_{1,h} > 0) \mathbf{B}_2$. From this expression, it is clear that alternating gradient descent algorithm for the BIP requires alternate back propagation through the generators \mathcal{B} , and \mathcal{C} as illustrated in Figure 3. To update \mathbf{h}_{t-1} , we fix \mathbf{m}_{t-1} , compute the Fourier transform of a scaling of the residual vector, and back propagate it through the generator \mathcal{B} . Similar update strategy is employed for \mathbf{m}_{t-1} keeping \mathbf{h}_t fixed.

4. Experiments and Results

We evaluate performance of proposed algorithm on three datasets; MNIST [18], street view house numbers (SVHN) [24], and CelebA [22]. Generator maps \mathcal{C} for MNIST and SVHN are trained on VAEs and for CelebA on GAN. All experiments including comparison methods are performed by adding 1%² Gaussian noise to blurry images \mathbf{y} .

Note that output of our proposed algorithm is constrained to lie in the range of generator. Since generator maps may not always correctly map to a low dimensional space *i.e.* they may not exactly produce an image \mathbf{x} belonging to \mathcal{X} , we define $\mathbf{x}_{\text{range}}$ that lie in range of generator \mathcal{C} and is closest image in ℓ_2 norm to any $\mathbf{x} \in \mathcal{X}$. Training of generative models is very important because a well trained \mathcal{B} and \mathcal{C} is capable of producing the entire \mathcal{X} and \mathcal{W} .

4.1. Blur Dataset and Generator

We generate two different synthetic blur datasets (A & B) using varying combinations of Gaussian and motion blurs.

Blur dataset A is modeled after camera shake blur and contains motion blurs with uniformly varying angle from 0 to 360 degrees with fixed length of 10. Blur dataset B contains centered overlapping Gaussian and motion blurs. The motion blurs in blur dataset B have the same specification as that of blur dataset A while Gaussian blurs are generated by varying standard deviation between 0.5 and 1.5. Visual depictions of both blur datasets is shown in Figure 4. We generate 80,000 blurs for each dataset and split them into 60,000 training and 20,000 test examples. Two different VAEs with same architecture are trained on training set of blur A and B, separately. After training, the generator \mathcal{B} (decoder in the case of VAE) is extracted and random samples from blur test set are used for evaluating performance of proposed algorithm. Length of blur feature vector \mathbf{h} is 50. Description of VAE architecture trained on blurs is given below.

Encoder. $\mathbf{w} \rightarrow C_2^{20} \downarrow 1 \rightarrow R \rightarrow \downarrow_2^2 \rightarrow C_2^{20} \downarrow 1 \rightarrow R \rightarrow \downarrow_2^2 \rightarrow \text{Flatten} \rightarrow D_{50}^L, D_{50}^L \rightarrow \mathbf{h}_{50}$

Decoder. $\mathbf{h}_{50} \rightarrow D_{720}^L \rightarrow R \rightarrow \text{Reshape} \rightarrow \uparrow_2 \rightarrow C_2^{20} \uparrow 1 \rightarrow R \rightarrow \uparrow_2 \rightarrow C_2^{20} \uparrow 1 \rightarrow R \rightarrow C_2^1 \uparrow 1 \rightarrow S \rightarrow \mathbf{w}$

where $C_a^b \downarrow s$ represents convolutional layer with b filters of size $a \times a$ and a stride of $s \times s$ and $C_a^b \uparrow s$ represents transposed convolutional layer with b filters of size $a \times a$ and a stride of $s \times s$. R and S represents rectified linear and sigmoid activation layers respectively, \downarrow_c^d represents a max pooling layer with a stride of $d \times d$ and pool size of $c \times c$ and \uparrow_c presents an upsampling layer with a size of $c \times c$. D_p^L represents a dense layer of size p with linear activation. $\mathbf{h}_{50} \in \mathbb{R}^{50}$ is the low dimensional feature representation of

²For an image scaled between 0 and 1, Gaussian noise of 1% translate to Gaussian noise with standard deviation $\sigma = 0.01$ and mean $\mu = 0$.

the blur kernels \mathbf{w} .

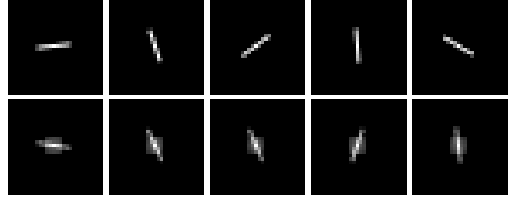


Figure 4: Blur Dataset. Sample kernels of size 28×28 from blur dataset A (row 1) and B (row 2)

4.2. Image Datasets

For all datasets; MNIST, SVHN and CelebA standard train and test data split is used in all experiments unless stated otherwise. MNIST dataset consists of 28×28 grayscale images of handwritten digits with 60,000 training and 10,000 test examples. VAE and GAN are reported to generate excellent images on this dataset [17] [11]. We train a variational autoencoder with convolution layers as the generative model for MNIST. Second dataset SVHN consists of $32 \times 32 \times 3$ real world images of house numbers obtained from google street view images. We use extra training dataset containing easy samples to train VAE. This set contained 531,131 examples, of which we chose 30,000 images as test set for evaluating performance and VAE is trained on remaining training images. CelebA dataset contains more than 200,000 RGB face images of size $218 \times 178 \times 3$ of different celebrities. We center crop the images to $64 \times 64 \times 3$ and scale them in range $[-1, 1]$ before feeding them into GAN for training as suggested by [29].

For all above datasets, images from test set were sampled and blurry images were produced by convolving with randomly sampled blur kernels from test sets of blur dataset A and B. Goal is to recover from these blurry images, the true sharp image and the blur kernel.

4.3. Blind Image Deblurring Results

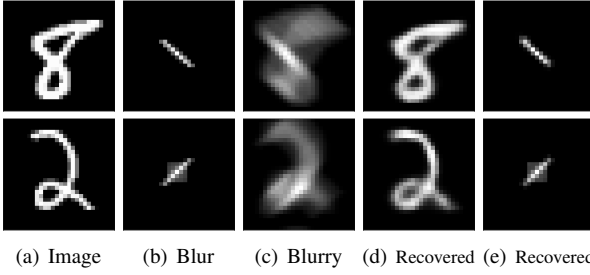
Deblurring for MNIST. For evaluating proposed blind image deblurring approach we first train VAE on training images of relatively simple dataset of MNIST. Batch size of 20 and learning rate of 0.00001 is used for training. Architecture for MNIST VAE is as follow.

Encoder. $\mathbf{x} \rightarrow C_3^{20} \downarrow 1 \rightarrow R \rightarrow \downarrow_2^2 \rightarrow C_3^{20} \downarrow 1 \rightarrow R \rightarrow \downarrow_2^2 \rightarrow \text{Flatten} \rightarrow D_{500}^L \rightarrow R \rightarrow D_{100}^L, D_{100}^L \rightarrow \mathbf{m}_{100}$

Decoder. $\mathbf{m}_{100} \rightarrow D_{500}^L \rightarrow R \rightarrow \text{Reshape} \rightarrow \uparrow_2 \rightarrow C_3^{20} \uparrow 1 \rightarrow R \rightarrow \uparrow_2 \rightarrow C_3^{20} \uparrow 1 \rightarrow R \rightarrow C_3^1 \uparrow 1 \rightarrow S \rightarrow \mathbf{x}$

where \mathbf{m}_{100} is the low dimensional feature representation for MNIST images with a length of 100.

Images from test set of MNIST are circularly convolved (point-wise multiplication in frequency domain) with blur



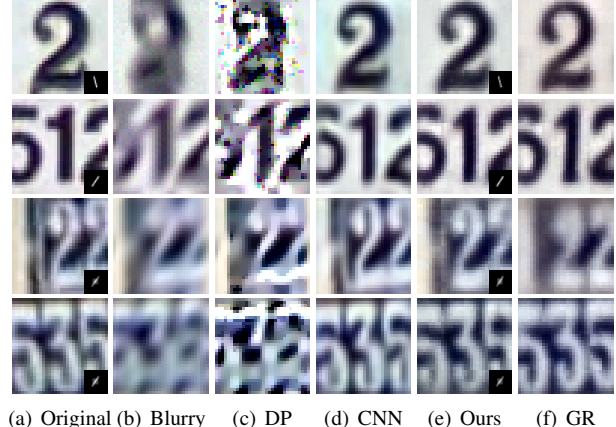
(a) Image (b) Blur (c) Blurry (d) Recovered (e) Recovered

Figure 5: Deblurring on MNIST. Images from MNIST (a) were convolved with blurs (b) to produce blurry images (c). (d) and (e) are the images recovered from the proposed approach.

kernels from test data sets of blur dataset A and B to produce blurry images \mathbf{y} . Alternating gradient descent is used to recover minimizers $\hat{\mathbf{m}}$ and $\hat{\mathbf{h}}$ of loss function in (6) by updating \mathbf{h} and \mathbf{m} alternatively in each iteration. Total number of iterations for alternating gradient descent is 1500 for MNIST. As gradient descent can get stuck in local minima so we employ 10 random restarts (trade off between accuracy and time) to initialize proposed algorithm for each restart by randomly initializing \mathbf{h} and \mathbf{m} from normal distribution and selecting the image and blur kernel with the minimum loss (7) as final estimate. We choose a decaying step size defined by $0.01e^{\frac{-t}{250}}$ where $t = 1, 2, \dots, 1500$ are number of iterations. The regularization penalty scaling factors are chosen to be $\gamma = 0.1$ and $\lambda = 0.1$ (found experimentally). Final deblurred image $\hat{\mathbf{x}}$ and blur $\hat{\mathbf{w}}$ are obtained by simply forward passing estimates $\hat{\mathbf{m}}$ and $\hat{\mathbf{h}}$ respectively, from input of generator to output. The Figure 5 shows true images, blur kernels, corresponding blurred images and the recovered images.

Base Line Methods. In the case of 1% Gaussian noise and blur size of 10, we choose dark prior (DP) [26] and CNN [12] as base line methods. Both of these have shown state of art performance in blind image deblurring task. Dark prior makes prior assumption on sparsity of dark channel of blurred image. We use default parameters in all experiments as they are already optimized for deblurring. We only fine tune maximum number of iteration that are 5 in original paper. We vary it between range 5 to 25 with step size of 3 and chose estimate with minimum error. [12] shows that convolutional neural networks (CNN) significantly outperforms state of the art methods for deblurring text documents images. We trained and fine tuned this network on CelebA and SVHN dataset separately with 150,000 training images each and 1% Gaussian noise. Like GAN we center crop the CelebA images to $64 \times 64 \times 3$ after resizing them for training of CNN.

Deblurring for SVHN. A VAE is trained on SVHN training dataset described in 4.2 with batch size of 64 and



(a) Original (b) Blurry (c) DP (d) CNN (e) Ours (f) GR

Figure 6: Deblurring on SVHN. Images from SVHN test set along with corresponding blur kernels are shown in (a) and the corresponding blurry image is given in (b). Recovery using dark prior (DP) and CNN is given in (c) and (d). (e) shows images recovered by proposed approach along with closest image in range (GR) shown in (f).

learning rate of 0.0001. The architecture of VAE trained on SVHN is described below.

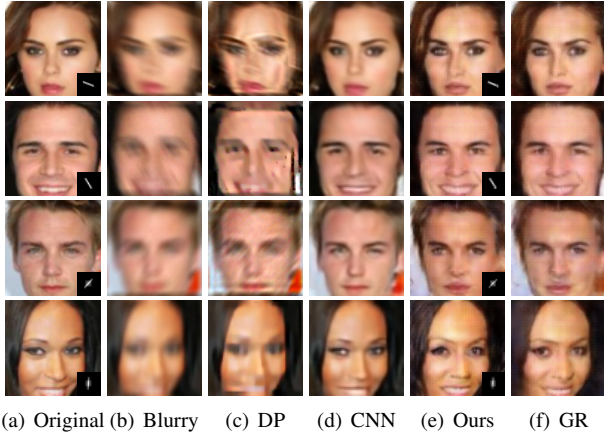
Encoder: $\mathbf{x} \rightarrow C_2^{128} \downarrow 2 \rightarrow \text{BN} \rightarrow R \rightarrow C_2^{256} \downarrow 2 \rightarrow \text{BN} \rightarrow R \rightarrow C_2^{512} \downarrow 2 \rightarrow \text{BN} \rightarrow R \rightarrow \text{Flatten} \rightarrow D_{100}^L, D_{100}^L \rightarrow \mathbf{m}_{100}$

Decoder: $\mathbf{m}_{100} \rightarrow D_{8192}^L \rightarrow \text{Reshape} \rightarrow C_2^{512} \uparrow 2 \rightarrow \text{BN} \rightarrow R \rightarrow C_2^{256} \uparrow 2 \rightarrow \text{BN} \rightarrow R \rightarrow C_2^{128} \uparrow 2 \rightarrow \text{BN} \rightarrow R \rightarrow C_1^3 \downarrow 1 \rightarrow S \rightarrow \mathbf{x}$

where, BN represent the batch normalization layer [14]. Images from test set were sampled randomly and blurred using blurs from Blur A and B test set. Proposed algorithm is used to recover the sharp image and the blur kernel. Total iteration used for gradient descent are 6,000 with decaying step size defined by $0.01e^{\frac{-t}{1000}}$ where $t = 1, 2, \dots, 6000$ with 10 random restarts. The regularization penalty scaling factor were chosen to be $\gamma = 0.1$ and $\lambda = 0.1$. The recovered sharp image and the blur kernel with corresponding blurry images is shown in Figure 6.

Deblurring for CelebA. We used DCGAN model of [27], as the generative model for CelebA images. Size of our low dimensional feature representation \mathbf{m} is 100. Model is trained by updating \mathcal{G} (proxy for \mathcal{C}) twice and \mathcal{D} once in each cycle to avoid fast convergence of \mathcal{D} . Each update used the Adam optimizer [16] with batch size 64, $\beta_1 = 0.5$, and learning rate 0.0002. For all experiments we use $\lambda = 0.001$ and $\gamma = 0.001$. Like in case of SVHN, we use 10 random restarts and choose estimate with minimum loss (7) as our final estimate. Gradient descent is used as optimizer with total iterations of 10,000 and a fixed step size of 0.001. Figure 7 shows the results obtained for CelebA.

Small Blurs. Quantitative results of deblurring CelebA



(a) Original (b) Blurry (c) DP (d) CNN (e) Ours (f) GR

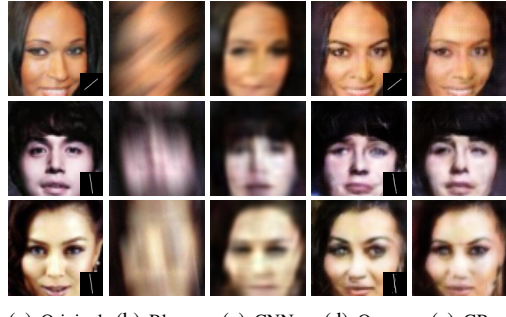
Figure 7: Deconvolution for CelebA. Images from CelebA test set along with corresponding blur kernels are shown in (a) and the corresponding blurry image is given in (b). Recovery using dark prior (DP) and CNN is given in (c) and (d). (e) shows images recovered by proposed approach along with closest image in generator range (GR) shown in (f).

Methods	DP	CNN	Ours
CelebA (Blur A)			
PSNR(dB)	19.674	28.338	23.525
SSIM	.781	.895	.822
SVHN (Blur B)			
PSNR(dB)	14.244	21.450	21.606
SSIM	.387	.869	.856
CelebA (Blur size 30)			
PSNR(dB)	-	19.441	20.072
SSIM	-	0.771	.784

Table 1: Quantitative comparison of proposed approach with dark prior (DP) and CNN for CelebA and SVHN dataset with blur test set A and B. We randomly sample 40 images from test set of CelebA and SVHN, 20 are blurred with blur A and 20 with blur B. This table shows average performance of PSNR and SSIM on these images.

and SVHN dataset with blur A and blur B in terms of Peak Signal to Noise Ratio (PSNR) and structural similarity Index (SSIM) [32] are given in Table 1. With blurs of size 10, CNN outperforms our proposed technique both in terms of PSNR and SSIM on CelebA dataset. On SVHN, CNN is only slightly better than our approach in terms of PSNR.

Robustness to Extravagant Blurs and Noise. To demonstrate the power of our algorithm on large blurs we train VAE on motion blur of size 30 having uniformly varying angle. Same architecture is used as in case of Blur A and B. We use this VAE as generator map \mathcal{C} for blurs and use previous GAN model trained on CelebA images as generator map \mathcal{B} for images. Dark Prior (DP) completely fails to estimate latent image for large blurs so we do not report its quantitative results. For CelebA, quantitative results are



(a) Original (b) Blurry (c) CNN (d) Ours (e) GR

Figure 8: Deconvolution with Large Blurs. Images from CelebA test set along with corresponding blur kernels are shown in (a). Corresponding blurry images (b) are recovered using CNN (c) and proposed approach (d) with the closest image in generator range (GR) shown in (e).

		Noise (%) →	10	20	30	40	50
		CelebA (Blur A)					
CNN	PSNR(dB) SSIM	16.556 0.621	14.216 0.407	13.450 0.334	12.275 0.220	11.772 0.174	
Proposed	PSNR(dB) SSIM	22.055 0.850	21.601 0.832	21.765 0.846	21.682 0.821	20.678 0.815	
SVHN (Blur A)							
CNN	PSNR(dB) SSIM	18.908 0.864	14.464 0.624	12.634 0.4893	11.747 0.308	10.803 0.2205	
Proposed	PSNR(dB) SSIM	24.765 0.967	20.823 0.930	20.963 0.935	15.120 0.778	13.213 0.733	

Table 2: Quantitative comparison in terms of PSNR and SSIM. Our proposed method outperform CNN for all noise level with significant margin.

presented in Table 1 which shows that in the regime of large blurs our algorithm outperforms CNN. Qualitatively results of our method are sharp and exhibit close resemblance with corresponding backpropagated images that lie in range of generator as shown in Figure 8. This shows robustness of our algorithm on extravagant blurs, where other algorithms tend to fail completely. The performance is only limited by generator as will be shown in Section 4.4.

For noise analysis, we compare our results with CNN. Both quantitative and qualitative results shows that our algorithm significantly outperforms CNN. CNN based approach works only good for noise level on which it is trained (1% gaussian noise here) and completely fails on other noise levels while our approach give impressive results even with 50% noise levels as shown in Figure 8. Quantitative results are shown in Table 2.

4.4. Range Error Analysis

Three sources of error exist: the feature representation \hat{h} and \hat{m} found by gradient descent may not always be the optimal ones, how far is the desired image x from the range

Methods	Test data error	Range space error
SVHN (Blur A)	0.00118	0.000501
SVHN (Blur B)	0.000993	0.000211
CelebA (Blur A)	0.000671	0.000290
CelebA (Blur B)	0.000823	0.000332

Table 3: Compare average (per pixel) reconstruction error for 50 images when recovering from a blurred image of range space images and test set images.

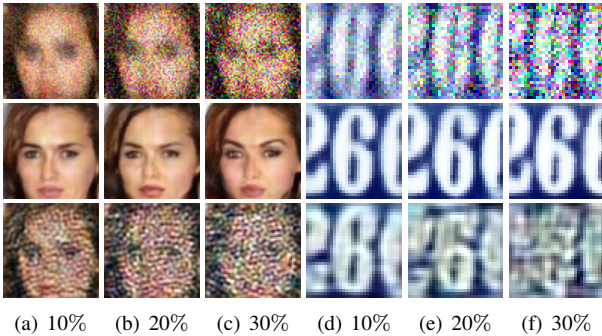


Figure 9: Noise Analysis. We show our recovered images (second row) from noisy blurred images (first row) and compare our results with [12] (third row). We vary the noise uniformly from 10% to 30%.

of the generator, and noise error. To reduce the first error, random restarts are used. As explained in [4], the dominant error is from the range of the generator. To demonstrate this affect, closest images in the range of the generator to the test images are found for both GAN and VAE. In case of GAN, we find closest image in the range of \mathcal{C} for a specific image in test set \mathbf{x}' , by minimizing its squared loss $\|\mathcal{C}(\mathbf{m}) - \mathbf{x}'\|^2$ with respect to latent variable \mathbf{m} by back propagation. We use 5 random restarts and 10,000 iterations with step size of 0.001 for finding the closest range image $\mathbf{x}_{\text{range}}$. In case of VAE, encoder is used to generate the latent representation corresponding to the test image. This latent representation is given to the decoder to generate the image in its range corresponding to the test image.

From these pairs of images, blurry images are generated, and then recover $\hat{\mathbf{x}}$ using proposed approach for each test and corresponding closest image in range. Using images from the range of \mathcal{C} guarantees that image being recovered lies in the range of the generator thus eliminating the second source of error. By comparing the average (per pixel) reconstruction error for images in range $\|\mathbf{x}_{\text{range}} - \hat{\mathbf{x}}\|_2$ against test set images $\|\mathbf{x}_{\text{test}} - \hat{\mathbf{x}}\|_2$ as shown in Table 3, it can be empirically seen that error for images in range space is much smaller than for images in test set which shows that generator with greater range can recover images exactly like test images and can perform many folds better.

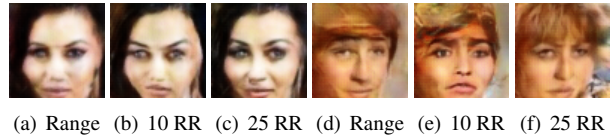


Figure 10: Failure case of recovering reconstructed image on large blur dataset. As clear from figure increasing number of random restarts (RR) can improve reconstruction accuracy significantly

5. Limitations

Currently, our approach is only limited by the range of generators \mathcal{B} and \mathcal{C} . GANs although capable of generating sharp and realistic looking images, they still lack in their generative capabilities. Most of the images in CelebA do not exactly lie in the range of the generator. A well trained generator with much greater range can recover exact images. We use 10 random restarts in all experiments. This value is found experimentally and by no mean close to optimum. Gradient descent can get stuck in local minima as shown in Figure 10 in which case more random restarts can improve performance. Moreover, fine tuning parameters of model and optimizer is also a challenge and need further investigation.

References

- [1] A. Aghasi, A. Ahmed, and P. Hand. Branchhull: Convex bilinear inversion from the entrywise product of signals with known signs. *arXiv preprint arXiv:1702.04342*, 2017. 3
- [2] A. Ahmed. *Low-rank matrix recovery: Blind deconvolution and efficient sampling of correlated signals*. PhD thesis, Georgia Institute of Technology, 2013. 3
- [3] A. Ahmed, B. Recht, and J. Romberg. Blind deconvolution using convex programming. *IEEE Transactions on Information Theory*, 60(3):1711–1732, 2014. 3
- [4] A. Bora, A. Jalal, E. Price, and A. G. Dimakis. Compressed sensing using generative models. *arXiv preprint arXiv:1703.03208*, 2017. 8
- [5] J.-F. Cai, H. Ji, C. Liu, and Z. Shen. Blind motion deblurring from a single image using sparse approximation. In *Computer Vision and Pattern Recognition, 2009. CVPR 2009. IEEE Conference on*, pages 104–111. IEEE, 2009. 3
- [6] E. J. Candes, Y. C. Eldar, T. Strohmer, and V. Voroninski. Phase retrieval via matrix completion. *SIAM review*, 57(2):225–251, 2015. 2
- [7] T. F. Chan and C.-K. Wong. Total variation blind deconvolution. *IEEE transactions on Image Processing*, 7(3):370–375, 1998. 3
- [8] O. Eches and M. Guillaume. A bilinear–bilinear nonnegative matrix factorization method for hyperspectral unmixing. *IEEE Geoscience and Remote Sensing Letters*, 11(4):778–782, 2014. 2

[9] R. Fergus, B. Singh, A. Hertzmann, S. T. Roweis, and W. T. Freeman. Removing camera shake from a single photograph. In *ACM transactions on graphics (TOG)*, volume 25, pages 787–794. ACM, 2006. 3

[10] I. Goodfellow. Nips 2016 tutorial: Generative adversarial networks. *arXiv preprint arXiv:1701.00160*, 2016. 3

[11] I. Goodfellow, J. Pouget-Abadie, M. Mirza, B. Xu, D. Warde-Farley, S. Ozair, A. Courville, and Y. Bengio. Generative adversarial nets. In *Advances in neural information processing systems*, pages 2672–2680, 2014. 3, 5

[12] M. Hradiš, J. Kotera, P. Zemcík, and F. Šroubek. Convolutional neural networks for direct text deblurring. In *Proceedings of BMVC*, volume 10, 2015. 2, 3, 6, 8

[13] Z. Hu, J.-B. Huang, and M.-H. Yang. Single image deblurring with adaptive dictionary learning. In *Image Processing (ICIP), 2010 17th IEEE International Conference on*, pages 1169–1172. IEEE, 2010. 3

[14] S. Ioffe and C. Szegedy. Batch normalization: Accelerating deep network training by reducing internal covariate shift. In *International Conference on Machine Learning*, pages 448–456, 2015. 6

[15] K. Jaganathan, Y. C. Eldar, and B. Hassibi. Phase retrieval: An overview of recent developments. *arXiv preprint arXiv:1510.07713*, 2015. 2

[16] D. Kingma and J. Ba. Adam: A method for stochastic optimization. *arXiv preprint arXiv:1412.6980*, 2014. 6

[17] D. P. Kingma and M. Welling. Auto-encoding variational bayes. *arXiv preprint arXiv:1312.6114*, 2013. 3, 5

[18] Y. LeCun. The mnist database of handwritten digits. <http://yann.lecun.com/exdb/mnist/>, 1998. 5

[19] A. Levin, Y. Weiss, F. Durand, and W. T. Freeman. Understanding and evaluating blind deconvolution algorithms. In *Computer Vision and Pattern Recognition, 2009. CVPR 2009. IEEE Conference on*, pages 1964–1971. IEEE, 2009. 3

[20] S. Ling and T. Strohmer. Blind deconvolution meets blind demixing: Algorithms and performance bounds. *IEEE Transactions on Information Theory*, 2017. 2

[21] S. Ling and T. Strohmer. Regularized gradient descent: A nonconvex recipe for fast joint blind deconvolution and demixing. *arXiv preprint arXiv:1703.08642*, 2017. 3

[22] Z. Liu, P. Luo, X. Wang, and X. Tang. Deep learning face attributes in the wild. In *Proceedings of the IEEE International Conference on Computer Vision*, pages 3730–3738, 2015. 2, 5

[23] S. Nah, T. H. Kim, and K. M. Lee. Deep multi-scale convolutional neural network for dynamic scene deblurring. *arXiv preprint arXiv:1612.02177*, 2016. 3

[24] Y. Netzer, T. Wang, A. Coates, A. Bissacco, B. Wu, and A. Y. Ng. Reading digits in natural images with unsupervised feature learning. In *NIPS workshop on deep learning and unsupervised feature learning*, volume 2011, page 5, 2011. 2, 5

[25] J. Pan, R. Liu, Z. Su, and G. Liu. Motion blur kernel estimation via salient edges and low rank prior. In *Multimedia and Expo (ICME), 2014 IEEE International Conference on*, pages 1–6. IEEE, 2014. 3

[26] J. Pan, D. Sun, H. Pfister, and M.-H. Yang. Blind image deblurring using dark channel prior. In *Proceedings of the IEEE Conference on Computer Vision and Pattern Recognition*, pages 1628–1636, 2016. 2, 3, 6

[27] A. Radford, L. Metz, and S. Chintala. Unsupervised representation learning with deep convolutional generative adversarial networks. *arXiv preprint arXiv:1511.06434*, 2015. 6

[28] W. Ren, X. Cao, J. Pan, X. Guo, W. Zuo, and M.-H. Yang. Image deblurring via enhanced low-rank prior. *IEEE Transactions on Image Processing*, 25(7):3426–3437, 2016. 3

[29] T. Salimans, I. Goodfellow, W. Zaremba, V. Cheung, A. Radford, and X. Chen. Improved techniques for training gans. In *Advances in Neural Information Processing Systems*, pages 2234–2242, 2016. 5

[30] C. J. Schuler, M. Hirsch, S. Harmeling, and B. Schölkopf. Learning to deblur. *IEEE transactions on pattern analysis and machine intelligence*, 38(7):1439–1451, 2016. 3

[31] I. Tasic and P. Frossard. Dictionary learning. *IEEE Signal Processing Magazine*, 28(2):27–38, 2011. 2

[32] Z. Wang, A. C. Bovik, H. R. Sheikh, and E. P. Simoncelli. Image quality assessment: from error visibility to structural similarity. *IEEE transactions on image processing*, 13(4):600–612, 2004. 7

[33] L. Xu, C. Lu, Y. Xu, and J. Jia. Image smoothing via 1 0 gradient minimization. In *ACM Transactions on Graphics (TOG)*, volume 30, page 174. ACM, 2011. 3

[34] X. Xu, D. Sun, J. Pan, Y. Zhang, H. Pfister, and M.-H. Yang. Learning to super-resolve blurry face and text images. In *Proceedings of the IEEE Conference on Computer Vision and Pattern Recognition*, pages 251–260, 2017. 3

[35] H. Zhang, J. Yang, Y. Zhang, and T. S. Huang. Sparse representation based blind image deblurring. In *Multimedia and Expo (ICME), 2011 IEEE International Conference on*, pages 1–6. IEEE, 2011. 3